CHINA FOUNDRY Research & Development
Vol. 23 No. 4 July 2026
www.springer.com/41230
https://doi.org/10.1007/s41230-026-4268-5

Process mechanisms for precision control in grayscale printing of additively manufactured sand molds

Gao-yang Yang[1, 2], *Zhong-de Shan[2, 3], **Li-ping Wang[1], ***Hao-qin Yang[2, 4], Dan-dan Yan[3], and Ya-jun Yin[5]

1. Department of Mechanical Engineering, Tsinghua University, Beijing 100084, China

2. State Key Laboratory of Advanced Forming Technology and Equipment, China Academy of Machinery Science and Technology, Beijing 100037, China

3. College of Mechanical and Electrical Engineering, Nanjing University of Aeronautics and Astronautics, Nanjing 210016, China

4. College of Material Science and Technology, Nanjing University of Aeronautics and Astronautics, Nanjing 210016, China

5. State Key Laboratory of Materials Processing and Die & Mould Technology, Huazhong University of Science and Technology, Wuhan 430074, China

Abstract: In purpose of solving the problem of precision deviation caused by droplet penetration in porous media during binder-jet printing of sand molds, the influence of process parameters such as sand mold printing grayscale and printing layer thickness on the performance and forming accuracy of 3D printed sand molds was systematically studied, and the causes of variations in tensile strength and *Z*-direction dimensional deviation were discussed in this study. The results show that the forming deviation in 3D printing sand molds is jointly affected by printing grayscale and printing layer thickness. When the printing layer thickness is the same, as the printing grayscale increases, the penetration distance of the binder increases, and the forming deviation also increases. When the printing grayscale is the same, as the layer thickness decreases, the forming deviation decreases. Under an optimized parameter setting with a layer thickness of 0.5 mm, the grayscale level of the near-surface layers reduces from 7 to 3. This leads to a 59% reduction in *Z*-direction dimensional deviation compared to using a grayscale level of 7 across all layers. This research result can provide a technical reference for high-precision sand mold printing and near-net forming of castings.

Keywords: sand mold 3D printing; forming accuracy; printing grayscale; layer thickness

CLC numbers: TG242 **Document code:** A **Article ID:** 1672-6421(2026)04-566-11

1 Introduction

As one of the main methods of metal forming, sand casting has been widely used in the field of equipment manufacturing[1, 2]. Against the general trend of market globalization, intensified competition in the manufacturing industry, accelerated product iteration, and shortened development cycles of new products, the complex process of traditional sand-casting technology is difficult to adapt to the production needs of newer and faster-moving products. Sand mold additive manufacturing processes and technologies have emerged in this context. Among them, sand mold 3D printing technology based on the droplet jet principle (3-dimension printing, 3DP) possess obvious advantages in single-piece, small-batch, and customized production scenarios. It also features higher production efficiency and lower material and equipment requirements than other sand mold additive manufacturing technologies. It has attracted widespread

***Zhong-de Shan**

Academician of the Chinese Academy of Engineering, Ph. D., Research Fellow and Doctoral Supervisor. His research interests mainly focus on digital mechanical equipment and advanced forming and manufacturing technologies and related equipment. He has published over 100 papers indexed by SCI, EI, and other databases and has authored five academic monographs. He holds more than 100 granted invention patents, including 38 international patents, and has received multiple awards for his research achievements, including two patents that received the China Patent Gold Award.

E-mail: shanzd@nuaa.edu.cn

****Li-ping Wang**

E-mail: wangliping@tsinghua.edu.cn

*****Hao-qin Yang**

E-mail: yang-haoqin@nuaa.edu.cn

Received: 2024-12-03; Revised: 2025-04-17; Accepted: 2026-03-13

attention and gained widespread favor from researchers, and has been put into wide application[3, 4]. Based on the CAD 3D model of the sand mold, sand mold 3D printing implements a discrete stacking, layer-wise manufacturing paradigm that enables the direct formation of molds and cores to meet casting process specifications. The technology reduces production time and cost, with required performance maintained, and offers a feasible pathway to near-net-shape forming and enhanced dimensional accuracy of printed sand molds[5-7].

In order to improve the ability to control the performance of printed sand molds, domestic and foreign researchers have carried out a series of research and development on sand mold 3D printing technology and equipment, and have achieved remarkable achievements in controlling the mechanical properties and forming accuracy of sand molds. Vaezi et al.[8] investigated the effects of sand layer thickness and binder content (by mass, wt.%) on the mechanical properties and dimensional accuracy of 3D printed sand molds. Under the same binder content, when the layer thickness decreased from 0.1 mm to 0.087 mm, the tensile strength of the sample increased, the bending strength decreased, and the surface quality and uniformity deteriorated. Zhao et al.[9] further conducted a representative investigation on the influence of multiple process parameters on printed sand molds, providing a useful reference for understanding parameter-property-accuracy relationships. In addition, other studies[10-15] have reported related effects of key factors, such as binder content, curing conditions, layer thickness, and particle characteristics, indicating that performance optimization typically requires coordinated parameter tuning rather than changing a single factor.

To interpret the above process-property observations, Ahmed and Sellier[16] modeled absorption-coupled spreading on porous substrates and showed that capillarity-driven transport was restrained by viscous dissipation and pore-scale resistance. Fu et al.[17] further numerically investigated droplet spreading and penetration on porous substrates, clarifying the coupled spreading-penetration behavior. These mechanistic insights, together with related mechanistic studies[18-21], provide a basis for process tuning, in which the selected layer thickness during slicing can be used to regulate binder transport and thereby influence dimensional deviation. Moreover, Maximenko et al.[22] analyzed how powder spreading can induce layer distortion and contribute to green-body dimensional errors. In the context of printed sand molds, Yang et al.[23] emphasized the importance of the sand-bed laying stage and discussed how spreading-related factors influence the resulting bed quality and forming accuracy.

Although sand mold 3D printing has progressed, achieving high dimensional accuracy without sacrificing mechanical performance remains difficult. Binder penetration, which is strongly affected by the selected layer thickness, often induces a strength-accuracy tradeoff, and variability in sand-laying quality further complicates control. To address this gap and provide mechanistic guidance for parameter tuning toward near-net shaping, the influence of process parameters such as printing layer thickness and printing grayscale on tensile strength and forming dimensional deviation was researched in this study.

2 Experimental methods and materials

2.1 Forming materials

This study employed silica sand for 3D printing provided by Beijing Deluke Technology Development Co., Ltd., with specifications of mesh number 100/200. According to the supplier's elemental analysis report, the content of the main component SiO_2 reached 99.54%, and each of the remaining components was below 0.15%, which met the needs of silica sand for printing[24]. The particle size distribution measured by the sieving method is shown in Fig. 1(a). The dominant size fraction was 106–150 μm (56.9%), and the median particle size (D_{50}) was approximately 139 μm. The microscopic image in Fig. 1(b) shows quartz grains that are mainly sub-angular to sub-rounded, indicating moderate sphericity and clean particle surfaces. The particles display a fairly narrow size spread around the sieve-measured peak, with limited fines and only occasional agglomeration.

SQ3D200 furan resin and the matching curing agent supplied by Jinan Shengquan Group were used. The furan resin is mainly composed of furfural, and the curing agent primarily consists of p-toluenesulfonic acid and concentrated sulfuric acid. The curing agent was premixed into the molding sand prior to printing.

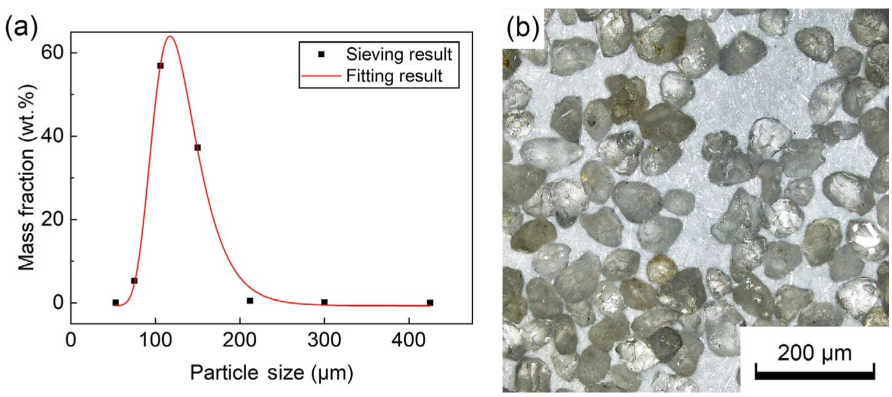

Fig. 1: Particle size distribution (a) and microscopic image of molding sand (b)

2.2 Forming equipment and method

The LSMP 600 sand mold 3D printing machine and supporting equipment developed by Beijing National Innovation Institute of Lightweight Ltd. were used to print samples. The appearance and internal forming space of the equipment are shown in Fig. 2.

The resin binder was firstly added to the liquid supply system of the sand mold printing and forming equipment, and was then replenished according to the usage. The curing agent was mixed with the raw sand at a mass ratio of 0.3:100, and then the blend was mixed in a sand mixer for 60 s until it was uniform to obtain the molding sand. The premixed molding sand was discharged from the sand mixer and temporarily stored in the molding sand bin for use.

The printing process parameters treated as variables were the printing grayscale (Levels 2–7) and layer thickness (0.3–0.7 mm). The remaining process parameters were kept constant in this study: print-head scanning speed of 500 mm·s^{-1}, sand-laying speed of 500 mm·s^{-1}, and both ink and ambient temperatures at 20 °C. Jetting resolution (dpi) and droplet characteristics were determined by the integrated commercial print head (Xaar 1003) and remained fixed throughout the experiments. As the grayscale level is not a direct measure of binder content, the actual binder jetting mass was calibrated for each grayscale level, and the corresponding binder content for each process parameter combination was derived from the calibration results. The binder content can be calculated using the following equation:

$$\omega_b = \frac{m_b}{m_b + \rho_s h \frac{N_{px}}{D_{px}}} \times 100\% \qquad (1)$$

where ω_b is the binder content (by mass, wt.%), m_b is the calibrated binder mass (g) corresponding to a given grayscale level, N_{px} is the total number of printed pixels in the calibration image, D_{px} is the areal pixel density determined by printing resolution *Res* (dpi) as $D_{px}=(Res/25.4)^2$, h is the printing layer thickness (mm), and ρ_s is the bulk density (g·cm^{-3}) of the laid molding sand, which was converted to g·mm^{-3} for calculation. The calculated results are shown in Table 1.

Printing proceeded on the LSMP 600 in a repeated cycle of sand laying and binder jetting until completion. For each layer, furan-resin binder was deposited along the sliced contour, the platform was lowered by one layer thickness, and a fresh sand layer was spread. This cycle was applied to all test samples (see Section 2.3), with the printing grayscale level and layer thickness depending on the group. Other printing parameters were kept constant as specified. The grayscale-to-binder content correspondence used in the analysis was obtained by jetting-volume calibration (Table 1). The binder content reported in Table 1 was obtained from calibration tests and subsequent calculation, and it was used as a reference for the actual binder content in printing.

2.3 Test-sample geometries

The experiments involved three types of printed sand-mold samples, as shown in Fig. 3. The dimensional-accuracy sample was a cubic block [Fig. 3(a)] used to quantify the

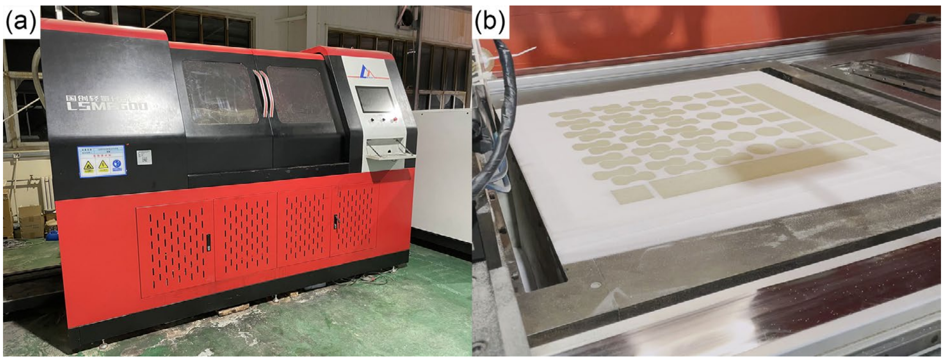

Fig. 2: LSMP600 sand-mold 3D printer (a) and binder-printed pattern on the sand-bed surface during printing (b)

Table 1: Calibration results of binder content

Grayscale level	7	6	5	4	3	2
Calibrated binder mass (g)	3.81	2.82	2.15	1.49	1.04	0.54
Layer thickness (mm)	Binder content (wt.%)					
0.3	6.07	4.55	3.77	2.35	1.47	0.98
0.4	4.55	3.41	2.83	1.76	1.10	0.74
0.5	3.64	2.73	2.26	1.41	0.88	0.59
0.6	3.03	2.28	1.88	1.18	0.73	0.49
0.7	2.60	1.95	1.61	1.01	0.63	0.42

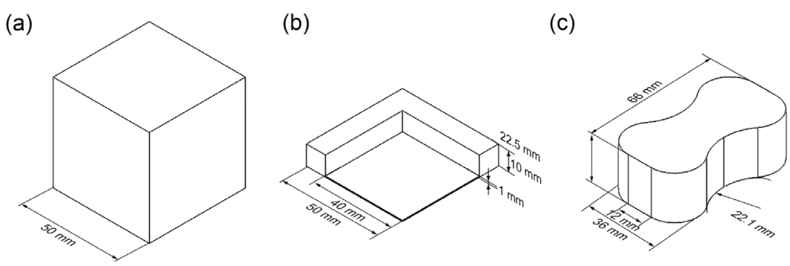

Fig. 3: Samples used in this study: (a) dimensional-accuracy sample; (b) infiltration sample; (c) tensile sample

dimensional deviation between the as-printed dimensions and the nominal CAD dimensions. The infiltration sample was a thin square plate with a supporting frame [Fig. 3(b)] used to measure the binder penetration depth in thin-plate sand-mold samples printed with a nominal thickness of 0.5–2 mm; under the investigated layer-thickness settings, the samples thickness corresponded to 1–4 layers. The tensile sample was an "8"-shaped sample conforming to GB/T 2684-2009[25] [Fig. 3(c)].

2.4 Post-processing methods

In this experiment, the printed sand mold was left to stand for 30 min until it was initially solidified and had sufficient handling strength. Then, the sand mold was taken out and placed in a drying oven at 120 °C for 60 min to complete curing. After oven curing, the sand mold was taken out of the oven and cleaned with compressed air and soft brushes to remove loosely bonded sand. During cleaning, a Shore hardness tester was used to monitor the surface hardness. When additional gentle brushing produced no change in the local Shore hardness reading, cleaning was considered complete and the cleaned surface was taken as the actual forming boundary.

2.5 Testing and characterization

2.5.1 Dimensional accuracy in *Z*-direction

To quantify the *Z*-direction forming deviation under different grayscale levels and layer thicknesses, precision-test samples were measured with a double-flat-jaw vernier caliper. For each sample, the *Z* dimension was measured from multiple orientations and compared with the nominal CAD value to obtain the *Z*-direction forming deviation. For each process condition, at least three samples were measured, and each sample was measured at least three times; the mean value was reported. Measurements adopted the forming boundary defined in Section 2.4.

2.5.2 Tensile strength

Tensile-test samples conforming to GB/T 2684-2009 were tested on an XQY-II intelligent sand-strength tester. For each process condition, at least three samples were tested, and the mean tensile strength was reported.

2.5.3 Microscopic observation of binder bridges

To assess the contributions of the near-surface forming layers and the extent of interlayer accumulation, a forming-deviation test was conducted on infiltration-test samples containing one to four deposited layers. The test covered grayscale levels of 3, 5, and 7 and layer thicknesses of 0.3, 0.5, and 0.7 mm. Each sample was a square thin-sheet block with a support frame, as shown in Fig. 2(b). Binder-bridge morphologies at interparticle contacts were examined under identical imaging settings to provide microstructural evidence for interpreting binder penetration and its relation to tensile strength and *Z*-direction forming deviation.

2.5.4 Infiltration-test for boundary forming layer deviation

To assess near-surface forming layer contributions and interlayer accumulation, a near-surface layer forming-deviation test was conducted on infiltration-test samples with one to four deposited layers at grayscale levels of 3, 5, and 7 and layer thickness of 0.3 mm, 0.5 mm, and 0.7 mm. Each sample followed the square thin-sheet with support-frame geometry shown in Fig. 2(b). After post-processing as defined in Section 2.4, the *Z* dimension was measured with a double-flat-jaw vernier caliper. Penetration distance and forming deviation in the *Z*-direction were compared across layer counts. Binder content for each combination of grayscale level and layer thickness was taken from Table 1.

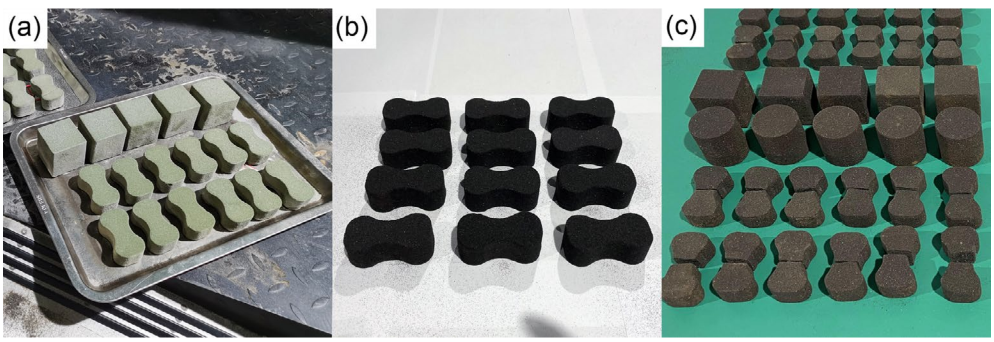

Fig. 4: Sand mold samples after printing: (a) initially taken out of the sand box; (b) after post-processing; (c) after test

2.5.5 Micro-CT scanning and interlayer porosity analysis

To further substantiate the mechanism underlying the dimensional-accuracy and strength trends, cubic blocks (10 mm×10 mm×10 mm) were cut from the precision-test samples for micro-CT scanning under three representative conditions: grayscale level 7 with layer thickness 0.5 mm, grayscale level 7 with layer thickness 0.7 mm, and grayscale level 3 with layer thickness 0.3 mm. All the three sample blocks were submitted for micro-CT scanning, scanning on a NanoVoxel-3000 micro-CT system with a nominal voxel size of 5 μm (commissioned to Tianjin Sanying Precision Instruments Co., Ltd.). The reconstructed slice stacks along the build *Z*-direction were used to segment internal pores and quantify the porosity profile and its periodicity along the *Z*-direction.

3 Experiment results

3.1 Influence of printing grayscale on printing results

The experiment results of the printed sand mold forming deviation test and tensile test are shown in Fig. 5.

With increasing printing grayscale, the *Z*-axis forming deviation rises [Fig. 5(a)], and the tensile strength shows the same overall increasing trend [Fig. 5(b)]. In the low-grayscale range (levels 2–4), the increase is approximately linear; once the grayscale enters the higher range (≥5), the rate of increase gradually decreases, indicating a tendency toward saturation at high jetting doses. The same monotonic increasing trend with increasing grayscale is observed at all tested layer thicknesses. A representative layer thickness of 0.5 mm was selected for illustration. This setting is commonly used on the machine and corresponds to the mid-point of the tested range from 0.3 to 0.7 mm. At the representative layer thickness of 0.5 mm, the relative increase in tensile strength decreases from 34.3% between grayscale levels 4 and 5 to 11.9% between levels 5 and 6, and further to 7.0% between levels 6 and 7 [Fig. 5(b)]. A similar reduction in incremental gain is observed at other tested thicknesses. These results suggest that further increasing the grayscale beyond level 5 yields only a limited additional improvement in tensile strength.

These trends can be interpreted by considering binder infiltration into the sand bed as flow through a porous medium. In a Darcy-type porous-media flow framework, a higher jetted dose provides a larger liquid supply and thus promotes deeper penetration before curing[26]. Because the binder content decreases with depth below the jetted surface, a gradient zone forms in which the bonding state transitions from strongly bonded to weakly bonded sand. During post-processing, the weakly bonded region is removed as loose sand, whereas the strongly bonded region survives cleaning and defines the effective forming boundary (Section 2.4). This mechanism explains the monotonic increase of *Z*-direction deviation and tensile strength with grayscale, as well as the diminishing returns at high grayscale levels observed in Fig. 5. Because only the boundary forming layers are adjusted, lowering the grayscale level in these layers is expected to weaken the near-surface bonding, whereas the load-bearing interior remains essentially unchanged; therefore, the overall tensile strength is expected to decrease slightly. For example, at a representative layer thickness of 0.5 mm, reducing the grayscale of the boundary forming layers from level 7 to level 3 decreases the *Z*-direction forming deviation by about 59% compared with the case where all layers use level 7 (Fig. 5).

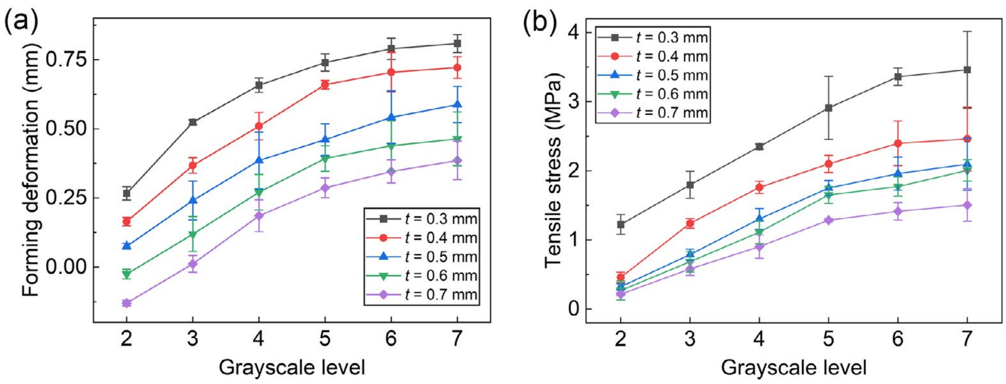

Fig. 5: Influence of grayscale levels on forming deviation (a) and tensile strength (b)

3.2 Influence of printing layer thickness on printing results

The experimental results above are re-plotted with the print layer thickness as the horizontal axis for display. The experimental results are shown in Fig. 6, grayscale level is abbreviated as GS.

From the experimental results shown in Fig. 6(a), it can be seen that with the increase of layer thickness, the forming deviation and tensile strength of the sand molds show a decreasing trend.

In sand mold printing, when the binder penetration distance in the *Z*-direction deviates from the target forming distance, the resulting difference is defined as the *Z*-direction forming deviation induced by process parameters. By processing the experiment data, the relationship between the printing layer thickness and the binder penetration distance can be obtained, as shown in Fig. 6(c). At a fixed grayscale level and with identical materials and processing conditions (sand,

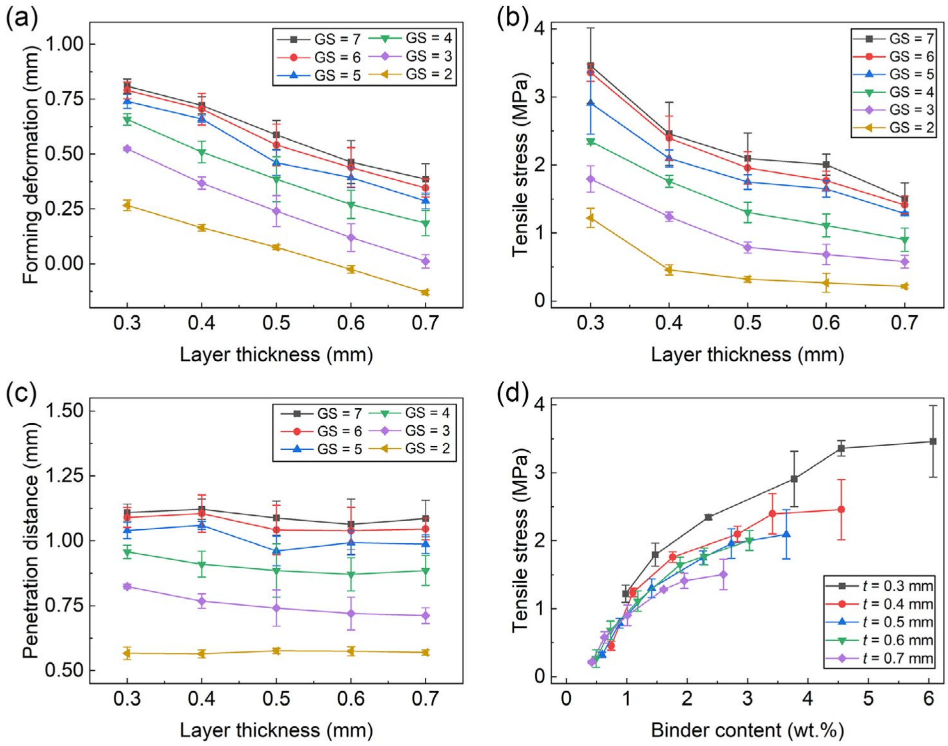

Fig. 6: Effect of forming layer thickness on forming deviation (a), tensile strength (b), and penetration distance (c); and effect of binder content on tensile strength (d)

binder, printing speed, and curing), it can be seen that with the increase of the printing layer thickness, the binder penetration distance has no obvious change. Therefore, the influence of the printing layer thickness on the *Z*-direction forming deviation in sand mold printing can be attributed to the change of the target forming distance introduced by slicing with a fixed layer thickness (layer-thickness rounding error). This deviation can be reduced by applying a small *Z*-direction boundary offset or scale factor during slicing.

According to the experimental results shown in Fig. 6(b), under the same printing grayscale conditions, as the layer thickness increases, the number of printed layers required to form the sand mold decreases, the binder content per unit volume decreases, the number and continuity of bonding bridges decrease, and the tensile strength shows a decreasing trend. The tensile strength curves with the binder content as the abscissa are shown in Fig. 6(d). The results show that, when the binder content is similar, the higher the layer thickness, the lower the tensile strength of the sand mold, indicating a less favorable binder distribution and degraded interlayer bonding at larger thickness. The strength of the sand mold is mainly determined by the number and state of the bonding bridges, which in turn depend on the binder content and its distribution. At the same binder content, when the layer thickness is large, regions with low binder distribution find it difficult to form enough bonding bridges to achieve enough interlayer bonding, and this lower bonding quality increases defects, making the sand mold strength lower.

By observing the appearance of the printed sand mold samples, it is found from Fig. 7 that at fixed layer thickness, the interlayer bonding quality on both the *XZ* and *YZ* surfaces of the sand mold deteriorates as the grayscale level decreases and layer-wise binder distribution stripes are clearly visible, arising from the grayscale-controlled jetting dose. As shown in Fig. 8, samples with low interlayer bonding quality cannot maintain bonding between layers during stretching. The fracture surface is uneven and exhibits irregular, layer-aligned serrations rather than discrete steps, which are consistent with failure influenced by interlayer defects, ultimately leading to lower tensile strength.

3.3 Analysis of penetration mechanism based on microscopic image observation

To further reveal the influencing mechanism of the printing grayscale, that is, the amount of binder injection, on the strength of the sand mold, a characterization study of the resin binder penetration process based on microscopic images was carried out.

In this section, microscopic observation was performed on penetration-test samples printed at a layer thickness of 0.5 mm with grayscale levels 2, 5, and 7. The optical microscopic images are shown in Fig. 9. It can be seen that the binder mainly forms bonding bridges at the contact points of the sand particles or between the smaller gaps. Within the investigated grayscale range, the locations of binder bridges remain similar, whereas the bridges become thicker and more interconnected as the grayscale increases.

When the binder content decreases, sand particles are in close contact but do not form bonding bridges [as indicated by the red arrows in Fig. 9(a)]. This indicates that the number of bonding bridges formed in the sand mold decreases and the strength of the sand mold decreases. The microscopic

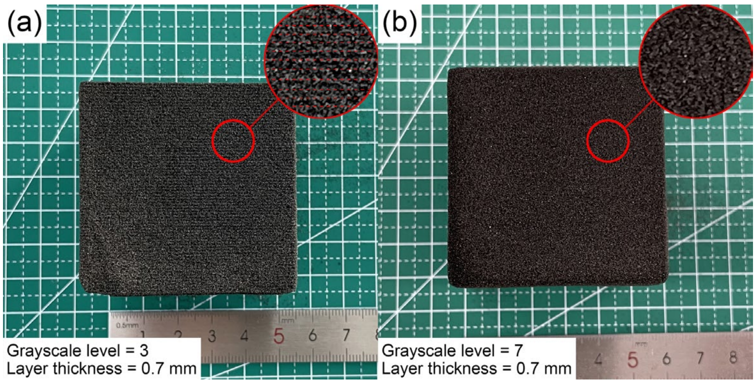

Fig. 7: Surface appearance of printed sand mold samples at low (a) and high (b) binder content

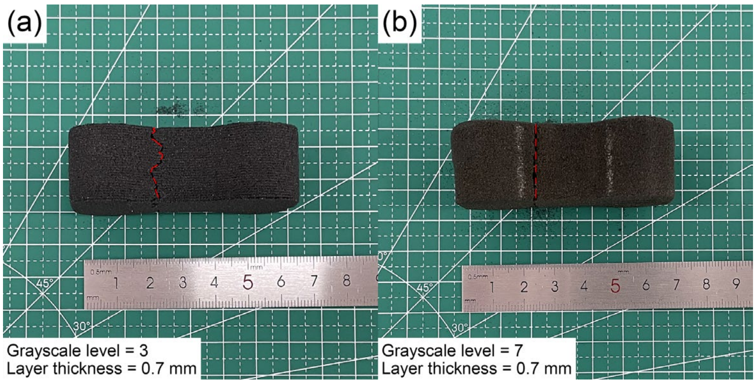

Fig. 8: Tensile fracture surfaces of printed sand mold samples at low (a) and high (b) binder content

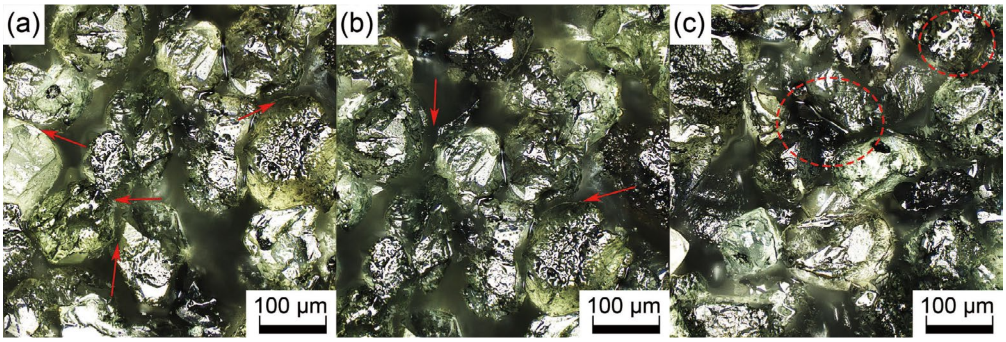

Fig. 9: Microscopic image observation results of penetration test samples: (a) grayscale level 2; (b) grayscale level 5; (c) grayscale level 7

bonding state between sand particles is governed by the liquid bridge formation, typically categorized as pendular state, funicular state, or capillary state[27, 28]. In this experiment, the observed bonding bridges formed under lower grayscale levels predominantly resemble the pendular state, where small binder volumes create discrete bridges between adjacent particles. As the binder content increases, partial bridges transform into a funicular state, where multiple particles are interconnected through continuous liquid channels. This transition enhances the internal connectivity and thus increases mechanical strength of the sand mold. However, features of binder pooling and continuous films, highlighted by the red circles in Fig. 9(c), are consistent with localized capillary state; accordingly, further increases in binder content provide little additional strength and may induce local defects such as over-bonded zones or uneven curing. This interpretation is consistent with the tensile test results: at a layer thickness of 0.5 mm, the relative increase in tensile strength drops markedly after grayscale level 5, decreasing from 34.3% between levels 4 and 5, to 11.9% between levels 5 and 6, and further to 7.0% between levels 6 and 7 [Fig. 5(b)].

3.4 Analysis of penetration mechanism based on infiltration test

This section analyzes the infiltration-test results (Section 2.5.4) across one to four forming layers for the 9 selected process combinations in Table 1 (grayscale levels 3, 5, and 7 with layer thicknesses 0.3, 0.5, and 0.7 mm). This section uses penetration distance as the measure, defined as the binder-driven change in thickness across the forming boundary and excluding the fixed slice-quantization offset introduced by layer-thickness rounding. The results are summarized in Fig. 10.

With increasing the number of forming layers, the penetration distance of the printed sample shows no obvious trend, that is, Figs. 10(a–c) show nearly flat trends and the small variations fall within measurement scatter, indicating no consistent relation between layer count and penetration distance. Accordingly, binder deposited in the current forming layer rarely passes through the previously formed surface into the underlying layer. Cross-layer penetration is minimal, and the penetration effect is dominated by the boundary forming layers.

Based on the experimental analysis, it can be inferred that the *Z*-direction penetration distance is governed mainly by the boundary forming layers, while contributions from adjacent layers are minimal. As shown in Figs. 10(a–c), the curves remain nearly flat across one to four layers, supporting the conclusion that cross-layer accumulation is negligible. This provides a practical way for regulating the *Z*-direction penetration behavior and subsequently controlling the *Z*-direction forming deviation of the sand mold. In practice, reducing the grayscale level during the printing of the boundary forming layers can minimize the forming deviation, while maintaining the grayscale level of interior forming layers unchanged helps maintain the overall strength of the sand mold [consistent with Fig. 5(b)].

As illustrated in Fig. 11, the mechanism can be summarized as follows. After the previous forming layer is printed, a binder-rich surface zone first forms on the surface of that layer, as shown in Fig. 11(a). The movement of the resin binder seeping into the molding sand is driven primarily by capillary pressure, while the hydrostatic head due to gravity is limited. When the penetration reaches the high binder concentration layer on the surface of the underlying (previous) forming layer, the partial capillary pressure caused by the gravity effect is less than the partial hydrostatic pressure caused by the binder concentration difference, so that the binder accumulates at the surface rather than penetrating further, as shown in Figs. 11(b) and (c). The binder distribution in the forming layer finally exhibits a pattern in which the binder content is higher near the upper and lower surfaces and lower in the middle, as shown in Fig. 11(d).

In this suppose, the binder mainly distributes at the surface and bottom of the sand layer, which can be explained by the capillary model in conjunction with the effects of gravity, wettability, viscosity, and curing rate. When the liquid comes into contact with the surface of the porous medium, capillary forces drive its penetration along the pores, which can be approximated by the Lucas-Washburn equation[29, 30]:

$$L(t) = \sqrt{\frac{\sigma r \cos\theta}{2\mu} t} \tag{2}$$

where $L(t)$ is the penetration depth, σ is the surface tension of the liquid, θ is the contact angle, r is the pore radius, and μ is the dynamic viscosity of the liquid.

This equation indicates that, in the initial stages, the penetration depth increases with the square root of time. However, the depth of liquid penetration is limited by the balance between capillary pressure and gravity, with the maximum penetration height (h_{max}) given by:

$$h_{max} = \frac{2\sigma \cos\theta}{\rho g r} \tag{3}$$

where ρ is the liquid density and g is the gravitational acceleration.

When capillary action dominates the initial penetration, the subsequent advance is controlled by the balance among the hydrostatic head due to gravity[31], the capillary entry pressure at interfaces, and viscous resistance along the pores.

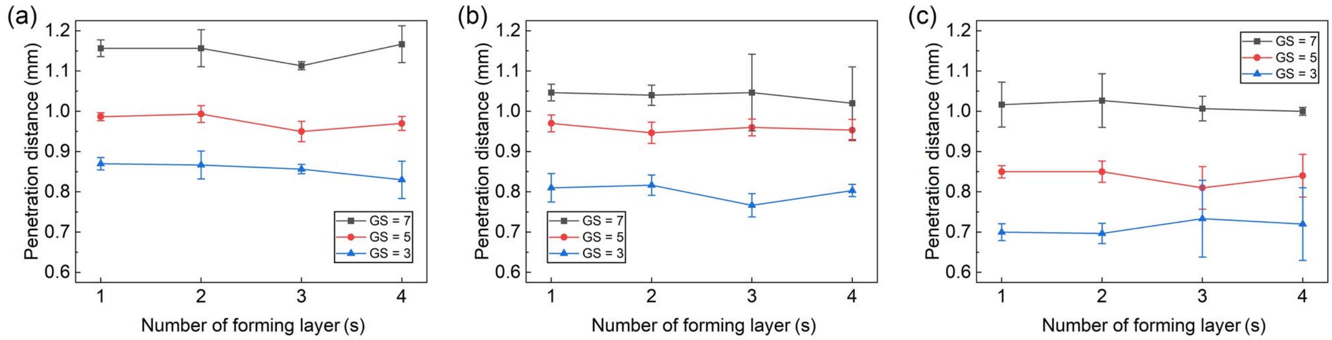

Fig. 10: Penetration distance test results: (a) 0.3 mm sample; (b) 0.5 mm sample; (c) 0.7 mm sample

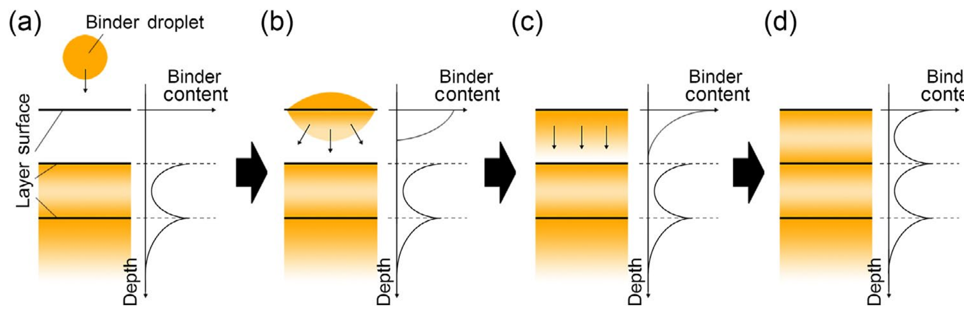

Fig. 11: Schematic diagram of interlayer penetration process of adhesive: (a) droplet falling; (b) diffusion increasing; (c) reaching the maximum diffusion area; (d) completed distribution

The Lucas-Washburn framework effectively captures early-stage penetration, and as binder content increases, capillary suction decreases and the vertical driving force weakens. When the hydrostatic head is lower than the capillary entry pressure at the underlying binder-enriched interlayer interface, the front may be hindered from crossing the interface and instead spreads laterally or accumulates at pore junctions, as illustrated in Figs. 11(b–c). The presence of surface tension gradients and early-stage partial curing further restricts deep infiltration. From a micromechanical standpoint, the formation of high-strength bonds depends on both the penetration depth and the consolidation of the binder at contact points. Rapid curing increases the local viscosity, solidifying the binder before uniform distribution is achieved, thus producing a heterogeneous bonding structure. From a microstructural perspective, the binder distribution is heterogeneous both within the *X*-*Y* plane and across successive layers. Along the *Z*-direction, the binder exhibits a periodic layering associated with layer-wise deposition and capillary redistribution. This non-uniformity contributes to the observed *Z*-direction forming deviation and may lead to direction-dependent strength between the *X*-*Y* plane (in plane) and *Z*-direction (build direction) [Fig. 11(d)].

Bottom accumulation, defined as the pooling of liquid binder at the lower interface, is primarily influenced by gravity and viscosity. During the penetration process, the liquid is driven into the medium by capillary forces and is constrained by Darcy's law, with the penetration rate *Q* described by the following relation:

$$Q = -\frac{k}{\mu}\nabla P \tag{4}$$

where k is the permeability of the porous medium, μ is the viscosity of the liquid, and ∇P is the pressure gradient. After the liquid enters the porous medium, gravity assists the downward flow. When the flow reaches a low-permeability or impermeable lower interface, for example, the cured surface of a previously printed layer, the vertical advance slows markedly unless the hydrostatic head exceeds the capillary entry pressure of that interface. The binder then accumulates at the lower interface and redistributes laterally. Additionally, the curing rate may influence the distribution of the binder: as the binder cures during penetration, its viscosity increases and hinders further downward flow. As a result, the binder may be retained at the interlayer surfaces, namely near the top surface of the current layer and at the lower surface that contacts the previously printed and cured layer, giving rise to a periodic pattern through the thickness.

In summary, the distribution of binder within the sand layer results from the combined effects of capillary forces, gravity, wettability, viscosity, and curing rate. The binder penetration behavior within the sand layer follows the Lucas-Washburn equation and tends to be enriched near the top surface and at the lower interface, with comparatively less in the middle, whereas bottom accumulation is governed by gravity and viscosity, particularly when printed sand layers are present at the bottom.

The experimental results show that the *Z*-direction penetration distance within the tested ranges of printing grayscale and layer thickness is mainly determined by binder penetration on the boundary forming layer, and shows no consistent relation with the penetration of other forming layers. By changing the printing grayscale for the boundary forming layers, the penetration distance can be turned to achieve the target thickness of these layers, thereby reducing the forming deviation of the sand mold.

3.5 Analysis of sand mold forming mechanism based on micro-CT scanning

The 3D reconstructions in Fig. 12 provide a qualitative view of the microstructure, while slice-wise analysis of the same dataset together with the associated statistics characterizes the through-thickness porosity and binder distribution, as shown in Fig. 13 and Table 2.

It can be seen from Fig. 13 that, except for the boundary parts near the bottom and top of the sand mold sample, the porosity distribution inside the sand mold shows obvious periodic fluctuations, and the fluctuation period is consistent with the layer-by-layer deposition period during the forming process.

In this section, interlayer denotes the interior portion of the Fig. 13 profiles obtained after removing the sharp variations at the beginning and the end of each curve. Porosity information inside the sand mold is listed in Table 2. It can be seen that the influence of the printing layer thickness on the overall porosity is relatively significant. The larger the printing layer thickness, the higher the porosity, and the larger the range of the internal-porosity variation. This increase in overall porosity and the widened range of internal porosity arise because increasing layer thickness degrades the laying quality (packing density) of the sand bed during spreading, which in turn elevates the overall porosity and amplifies the slice-to-slice variation. The binder content in the molding sand is relatively small (0.88wt.%–3.64wt.%, Table 2) and is therefore not the main determinant of porosity. During forming, a thicker printed layer together with reduced packing density lengthens the penetration path and increases the flow resistance for the binder, leading to a more non-uniform through-thickness binder distribution in the sand mold. At a fixed grayscale level of 7, increasing layer thickness from 0.5 to 0.7 mm increases the internal porosity range, consistent with a more non-uniform through-thickness binder distribution. A sand mold with a non-uniform binder distribution shows lower internal strength consistency, and is more prone to delamination and fracture when subjected to stress, resulting in lower final strength.

It can also be seen from Table 2 that, at a fixed layer thickness, the printing grayscale also has an effect on the porosity distribution inside the sand mold. A higher grayscale is associated with a smaller internal porosity range (maximum minus minimum internal slice porosity; see Table 2). This indicates a more uniform through-thickness binder distribution driven by stronger capillary penetration, leading to higher internal-strength consistency and a lower propensity for fracture and hence a higher final strength.

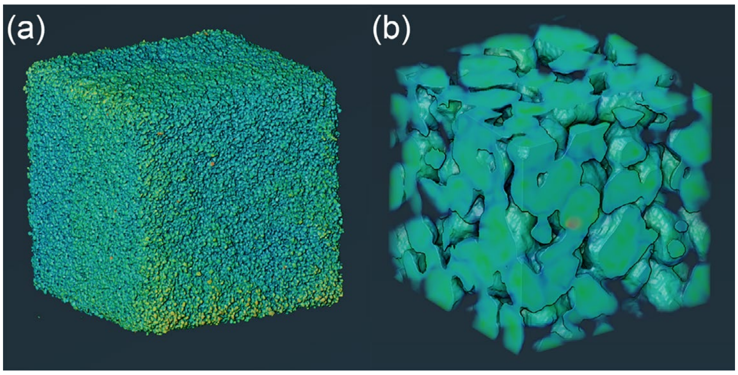

Fig. 12: Reconstructed model from micro-CT scanning results: (a) full scanned model; (b) part of the internal model

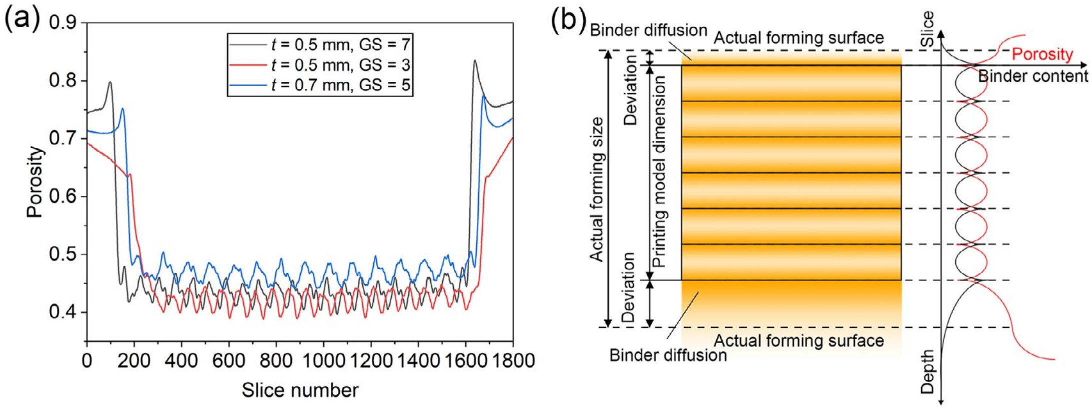

Fig. 13: Micro-CT scanning results for porosity analysis (a) and schematic diagram of porosity distribution (b)

Table 2: Porosity information inside the sand mold

	Layer thickness 0.5 mm Grayscale level 7	Layer thickness 0.5 mm Grayscale level 3	Layer thickness 0.7 mm Grayscale level 7
Binder content (wt.%)	3.64	0.88	2.6
Average internal porosity	0.425	0.435	0.468
Minimum internal slice porosity	0.399	0.370	0.382
Maximum internal slice porosity	0.478	0.479	0.489
Internal porosity range (max-min among interior slices)	0.078	0.109	0.107

Overall, the micro-CT evidence indicates higher packing density at the surfaces of each forming layer. Quantitative slice-wise analysis of the same dataset (Fig. 13), together with the statistics in Table 2, reveals a periodic through-thickness pattern: binder preferentially accumulates at the interlayer surfaces, with relative depletion in the middle of the layer. This distribution is consistent with capillary-driven penetration limited by pore-scale viscous resistance and the capillary entry pressure at the lower interface. These constraints suppress vertical advance and promote binder accumulation at interlayer surfaces, in agreement with the penetration mechanism discussed in Sections 3.3–3.4.

4 Conclusions

This study quantifies how grayscale level and layer thickness affect the dimensional accuracy and tensile strength of binder-jet-printed sand molds. The main conclusions are:

(1) Printing grayscale has a significant effect on the *Z*-direction forming deviation in the printed sand mold and the effect of layer thickness is even stronger. Micro-CT slice-wise analysis shows binder accumulation at interlayer surfaces and a periodic through-thickness pattern; at the same grayscale, increasing the layer thickness enlarges the through-thickness porosity variation and raises the average porosity. Therefore, using smaller grayscale levels in combination with appropriately thin layers helps reduce the forming deviation.

(2) In droplet-based binder-jet printing of sand molds, at a 0.5 mm layer thickness, the tensile strength increases with the grayscale level but approaches a plateau around level 5. Increasing the grayscale level further provides only marginal gains, in line with micrographic evidence of surface pooling

and film formation.

(3) By reducing the grayscale level in the boundary forming layers of the sand mold, penetration distance beyond the mold edge in the Z-direction can be minimized, thereby reducing the forming deviation. According to the experimental results presented in this study, at a layer thickness of 0.5 mm, reducing boundary layer grayscale level from level 7 to level 3 results in a 59% reduction in the Z-direction forming deviation. This reduction facilitates algorithm-based dimensional control and supports near-net shaping.

Acknowledgments

This work was financially supported by the National Key R&D Program of China (No. 2021YFB3401200), the Jiangsu Provincial Basic Research Program (Natural Science Foundation) Youth Fund (No. BK20230885), the International Joint Laboratory of Sustainable Manufacturing, Ministry of Education and the Fundamental Research Funds for the Central Universities (No. NG2024012), and the State Key Laboratory of Materials Processing and Die & Mould Technology, Huazhong University of Science and Technology (No. P2024-007).

Conflict of interest

The authors declare that they have no conflict of interest.

References

[1] Shan Z D. Patternless casting, Vol. 1. Beijing: China Machine Press, 2017: 69. (In Chinese)

[2] Chadha U, Dhaliwal G S, Sondi N J, et al. Optimization of process parameters and additives for improved part quality in sand casting: An overview. Journal of The Institution of Engineers (India): Series D, 2025, 106(2): 1289–1313.

[3] Le Néel T A, Mognol P, Hascoët J Y. A review on additive manufacturing of sand molds by binder jetting and selective laser sintering. Rapid Prototyping Journal, 2018, 24(8): 1325–1336.

[4] Hackney P M, Wooldridge R. Characterisation of direct 3D sand printing process for the production of sand cast mould tools. Rapid Prototyping Journal, 2017, 23(1): 7–15.

[5] Yan D D. Study on the precision and performance regulation technology of multi-material composite sand mold by 3D printing. Doctoral Dissertation, University of Science and Technology Beijing, 2023. (In Chinese)

[6] Kang L W, Wang M, Zou Y F. The influence of modifiers on the properties of furan resin sand. Foundry, 2020, 69(3): 259–262. (In Chinese)

[7] Sivarupan T, Balasubramani N, Saxena P, et al. A review on the progress and challenges of binder jet 3D printing of sand moulds for advanced casting. Additive Manufacturing, 2021, 40: 101889.

[8] Vaezi M, Chua C K. Effects of layer thickness and binder saturation level parameters on 3D printing process. The International Journal of Advanced Manufacturing Technology, 2011, 53(1–4): 275–284.

[9] Zhao H P. Study on the key technology of rapid forming casting molds and cores by micro-jetting and bonding. Doctoral Dissertation, Huazhong University of Science and Technology, 2015. (In Chinese)

[10] Khandelwal H, Ravi B. Effect of molding parameters on chemically bonded sand mold properties. Journal of Manufacturing Processes, 2016, 22: 127–133.

[11] Sivarupan T, El Mansori M, Coniglio N, et al. Effect of process parameters on flexure strength and gas permeability of 3D printed sand molds. Journal of Manufacturing Processes, 2020, 54: 420–437.

[12] Chate G R, Patel G C M, Deshpande A S, et al. Modeling and optimization of furan molding sand system using design of experiments and particle swarm optimization. Proceedings of the Institution of Mechanical Engineers, Part E: Journal of Process Mechanical Engineering, 2018, 232(5): 579–598.

[13] Acharya S G, Vadher J A, Kothari K D. Evaluation of critical parameters for sand inclusion defect in FNB casting. Archives of Foundry Engineering, 2017, 17(1): 5–12.

[14] Dana H R, El Mansori M. Mechanical characterisation of anisotropic silica sand/furan resin compound induced by binder jet 3D additive manufacturing technology. Ceramics International, 2020, 46(11): 17867–17880.

[15] Coniglio N, Sivarupan T, El Mansori M. Investigation of process parameter effect on anisotropic properties of 3D printed sand molds. The International Journal of Advanced Manufacturing Technology, 2018, 94(5–8): 2175–2185.

[16] Ahmed G, Sellier M. Modeling the effects of absorption on spreading dynamics. Transport in Porous Media, 2016, 112(3): 637–663.

[17] Fu F, Li P, Wang K, et al. Numerical simulation of sessile droplet spreading and penetration on porous substrates. Langmuir, 2019, 35(8): 2917–2924.

[18] Ahmed G, Arjmandi Tash O, Cook J, et al. Biological applications of kinetics of wetting and spreading. Advances in Colloid and Interface Science, 2017, 249: 17–36.

[19] Van Gaalen R T, Diddens C, Siregar D P, et al. Absorption of surfactant-laden droplets into porous media: A numerical study. Journal of Colloid and Interface Science, 2021, 597: 149–159.

[20] Yu H, Son G, Shim W. Numerical simulation of droplet merging and chemical reaction in a porous medium. International Communications in Heat and Mass Transfer, 2017, 89: 154–164.

[21] Li Z, Shan Z D, Sun Q L. Influence mechanism of resin penetration on molding accuracy of sand 3D printing. Foundry Technology, 2021, 42(4): 247–251. (In Chinese)

[22] Maximenko A L, Olumor I D, Maidaniuk A P, et al. Modeling of effect of powder spreading on green body dimensional accuracy in additive manufacturing by binder jetting. Powder Technology, 2021, 385: 60–68.

[23] Yang W, Qian Z, Xian H, et al. Research on roller size modeling of sand bed laying in 3DP process. Manufacturing Technology & Machine Tool, 2023, 6: 5–10. (In Chinese)

[24] GB/T 9442-2010. Foundry silica sand. Beijing: Standards Press of China, 2010. (In Chinese)

[25] GB/T 2684-2009. Test methods for foundry sands and molding mixtures. Beijing: Standards Press of China, 2009. (In Chinese)

[26] Cheng Y L, Li Y T, Yang Y T, et al. Greyscale printing and characterization of the binder migration pattern during 3D sand mold printing. Additive Manufacturing, 2022, 56: 102929.

[27] Mitarai N, Nori F. Wet granular materials. Advances in Physics, 2006, 55(1–2): 1–45.

[28] Lian G, Thornton C, Adams M J. A theoretical study of the liquid bridge forces between two rigid spherical bodies. Journal of Colloid and Interface Science, 1993, 161(1): 138–147.

[29] Fries N, Dreyer M. An analytic solution of capillary rise restrained by gravity. Journal of Colloid and Interface Science, 2008, 320(1): 259–263.

[30] Washburn E W. The dynamics of capillary flow. Physical Review, 1921, 17(3): 273–283.

[31] Mason G, Morrow N R. Capillary behavior of a perfectly wetting liquid in irregular triangular tubes. Journal of Colloid and Interface Science, 1991, 141(1): 262–274.